

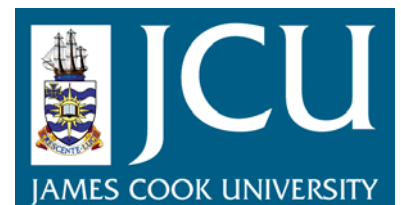
JCU ePrints

This file is part of the following reference:

McLellan, John George (2004) *Numerical modelling of deformation and fluid flow in hydrothermal systems.* PhD thesis, James Cook University.

Access to this file is available from:

<http://eprints.jcu.edu.au/2131>



Numerical Modelling of Deformation and Fluid Flow in Hydrothermal Systems

Thesis submitted by

John George McLellan B.Sc. (Hons.1st class, JCU)

October 2004

for the degree of Doctor of Philosophy in

the Department of Earth Sciences

James Cook University, North Queensland

STATEMENT OF ACCESS

I, the undersigned, author of this work, understand that James Cook University will make this thesis available for use within the University Library and, via the Australian Digital Theses network, for use elsewhere.

All users consulting this thesis will have to sign the following statement:

“In consulting this thesis I agree not to copy or closely paraphrase it in whole Or in part without the written consent of the author; and to make proper public written acknowledgment for any assistance that I have obtained from it.”

I understand that, as an unpublished work, a thesis has significant protection under the Copyright Act and;

I wish this work to be embargoed until: 1st October 2005

Signature

Date

STATEMENT OF SOURCES**DECLARATION**

I declare that this thesis is my own work and has not been submitted in any form for another degree or diploma at any university or other institution of tertiary education. Information derived from the published or unpublished work of others has been acknowledged in the text and a list of references is given.

Signature

Date

STATEMENT OF CONTRIBUTIONS

General contributions towards this study have included:

- Australian Post Graduate Award (APA) scholarship
- pmd*CRC top-up scholarship
- pmd*CRC educational and training fund
- ARC large grant to Oliver & Dickens, financial support towards Chapter 3

Contributions from others towards this thesis have been clearly stated at the forefront of each chapter where applicable, and these people and their contributions to this study include the following:

Chapter 3: P.M. Schaub – assistance with computer codes relating to the FISH functions for FLAC

Chapter 4: L.Feltrin – 3D Modelling of the Century Deposit and text including the following contribution: 20% (p. 88-103), 50% (p. 67-77, 103-106), and 80% (p. 88-103)

Chapter 6: N.H.S. Oliver – Conceptual ideas for this chapter, background research and text including the following: 90% (p. 147-153), and 10% (p. 153-163)

And normal supervisory conditions throughout the course of this study by

N.H.S. Oliver

AKNOWLEDGEMENTS

I would like to thank my principal supervisor, Nick Oliver for his enthusiasm, dedication and patience in this project. I thank him for his assistance and his willingness to discuss many aspects of this work, and also many suggestions that helped improve this thesis. I also thank my external supervisor Alison Ord (CSIRO) for discussions and problem solving in relation to the modelling work carried out. I would also like to thank Bruce Hobbs and the team at CSIRO Exploration and Mining (Computational Geoscience) for giving me feedback on many problems I encountered along the way, and a special note of thanks to Mike Coulthard for prompt assistance from ITASCA.

Many thanks go out to all who participated in discussions during the course of this study and some of these people include (in alphabetical order): Tom Blenkinsop, Matt Brown, James Cleverley, Leonardo Feltrin, Damien Foster, Jeff Loughran, Geordie Mark, Lucas Marshall, Roger Mustard, Peter Schaub, Adam Webb and Yanhua Zhang. A special note of thanks goes out to all of the members of the pmd*CRC for encouragement and discussion at conferences and annual reviews.

Finally I would most like to thank my family and friends, for being who they are, and for helping me become the person I am. I am eternally grateful.

Abstract

Geomechanical processes involved in mineralisation of several Australian deposits were tested using both continuous and discontinuous modelling techniques. Numerical modelling using both the finite difference method and discrete element method, were carried out by firstly devising conceptual models. This also allowed rigorous sensitivity testing of many input parameters throughout the modelling procedure. Fully coupled deformation and fluid flow modelling was applied to investigate and establish the influence of topography, structure and extension on porous media fluid flow. Iron ore genesis in the Hamersley Province, W.A., has been a contentious genetic issue for many years, with several ore genesis models proposed. Modelling results from this study confirm the mechanical feasibility of focusing both surface and basinal derived fluids towards sites of iron ore genesis during Proterozoic orogenic collapse, providing upward and downward migration of (reduced and oxidised) fluids during deformation, and allowing infiltration of banded iron formations and consequent silica loss during permeability increase, resulting in favourable conditions for ore genesis.

Extension and contractional models of potential scenarios of ore emplacement at the Century Zn-Pb-Ag deposit in northwest Queensland were tested by a combination of 3-D structural modelling and fully coupled fluid flow models. Three conceptual models were devised, and two of these were fully tested by numerical simulations (diagenetic and epigenetic), the other (syngenetic) by Geological Computer Aided Design (GoCad). Reconstruction of the 3-D structural model displayed thickness and grade relationships to NE trending growth faults, providing evidence that supports a syngenetic model of

emplacement. Numerical models provide clear evidence that stratiform Zn-Pb mineralisation is difficult to achieve in subsurface conditions, due to the low permeability of shale units. During contractional deformation, modelling results suggest that it would most probably result in fault or vein style mineralisation at the Century deposit, due to the proximal nature of fluid focussing relative to the faults.

*The Eastern Succession of the Mt Isa Inlier is a mineral rich region, with many large deposits such as Cannington Pb-Zn-Ag, Osborne Cu-Au, and Selwyn Cu-Au. This area has been the focus of mineral exploration for some years, and evaluating the prospectivity of this region is one of the current goals of the pmc*CRC. Stress partitioning in this region, during the Isan Orogeny, may have played a vital role in determining the locations of mineral deposits as a result of failure and fluid flow. Discrete element modelling of the Eastern Succession provides strong correlations with known ore deposits and prospects, particularly in the Selwyn region, and also provides several testable targets. Comparisons of these results correspond well with other current prospectivity analysis of the region. The results indicate that mineralising fluids were preferentially focussed into zones of anomalous stress in and around fault zone bends and intersections, and intrusive metasediment contacts. Furthermore the optimum far-field stress that provides the best correlation with known deposit distribution was orientated E/SE rather than E/W, suggesting a component of regional transpression late in the 1600 – 1500 Ma Isan Orogeny.*

Extension related mineralisation is commonly linked to near surface fluids penetrating into deeper parts of the crust and possible fluid mixing occurring. The general mechanics of extensional faulting are fairly well understood at a

range of scales, and many models have been proposed. Hydrodynamic models, however, are considerably fewer. This study applied fully coupled deformation and fluid flow numerical models to test the role of extensional deformation and its effects on fluid flow, particularly at basement-cover interfaces. Large contrasts in the permeability of the basement and cover restrict fluid exchange between these two units, unless permeable faults or shear zones are present. Downward migration of fluids is a natural consequence of the extension of dilatant materials where strain rates are high. Rapid decreases in pore pressure, as a result of dilation and failure, may provide mechanisms for mass transfer across basement cover interfaces.

TABLE OF CONTENTS

- Title page
- Statement of Access
- Statement of Sources
- Statement of Contributions
- Acknowledgements
- Abstract
- Table of Contents
- List of Figures
- List of Tables
- List of Symbols

SECTION A

Chapter 1: Introduction	p.	1
1.1 General Introduction	p.	2
1.2 Numerical Modelling Applications	p.	3
1.3 Aims & Objectives	p.	3
1.4 Thesis Outline	p.	4
1.4.1 Section A	p.	4
1.4.2 Section B	p.	6
Chapter 2: Numerical Modelling	p.	7
2.1 Introduction	p.	8
2.2 Theoretical Background	p.	9
2.2.1 General mechanical Relationships	p.	9
2.2.2 Elastic-Plastic Behaviour	p.	14
2.2.2.1 Elasticity	p.	16
2.2.2.2 Plasticity	p.	18
2.2.3 Constitutive Models	p.	25
2.2.4 Porous Media & Fluid Flow	p.	26
2.2.5 Fluid Behaviour & Discrete Fractures	p.	37
2.3 Modelling Process	p.	40
2.3.1 Numerical Procedure	p.	41
2.4 Modelling Approaches & Software	p.	44
2.4.1 Continuum & Discontinuum Methods	p.	44
2.4.2 FLAC	p.	45
2.4.3 UDEC	p.	48

Chapter 3: Hamersley Province	p.	51
<i>Abstract</i>	p.	52
3.1 Introduction	p.	53
3.2 Hamersley Province	p.	57
3.2.1 Structural History	p.	58
3.2.2 Ore Genesis Models & Fluid Flow History	p.	60
3.3 Theoretical Background / Mechanical Modelling	p.	62
3.3.1 Finite Difference Code	p.	62
3.3.2 Mechanical Relationships	p.	63
3.3.3 Fluid Flow Theory	p.	64
3.3.4 Deformation & Fluid Flow Coupling	p.	65
3.4 Boundary Conditions & Model Parameters	p.	66
3.4.1 General Conditions	p.	66
3.4.2 Hamersley Specific Models	p.	69
3.5 Model Results	p.	72
3.5.1 Model 1	p.	72
3.5.2 Model 2	p.	73
3.5.3 Model 3	p.	74
3.5.4 Model 4	p.	75
3.5.5 Model 5	p.	77
3.5.6 Model 6	p.	79
3.5 Discussion & Conclusions	p.	81
Chapter 4: Century Deposit	p.	85
<i>Acknowledgements</i>	p.	86
<i>Abstract</i>	p.	87
4.1 Introduction	p.	88
4.2 Tectonic Evolution & Stratigraphic Subdivisions	p.	93
4.2.1 The Mount Isa Inlier	p.	93
4.2.2 The Western Fold Belt	p.	96
4.2.3 Stratigraphy of the Lawn Hill Formation	p.	99
4.3 Century Deposit	p.	104
4.3.1 Sulphide Textures	p.	104
4.3.2 Ore Zone Stratigraphy	p.	105
4.4 Introduction to 3D Structural Modelling	p.	108
4.4.1 GoCad	p.	109
4.4.2 Initial Steps to Construct a 3D Model	p.	111
4.4.3 Data Acquired to Construct a 3D Model	p.	112
4.4.4 3D Model Components	p.	112
4.4.5 3D Modelling Results	p.	113
4.5 Century Ore Genesis	p.	120
4.6 Deformation & Fluid Flow	p.	126
4.7 Numerical Modelling	p.	128
4.7.1 FLAC	p.	129

4.7.2	Sensitivity of Strain Rates	p. 129
4.7.3	Conceptual Models	p. 131
4.7.4	Conceptual Model 1	p. 133
4.7.5	Conceptual Model 2	p. 135
4.8	Results	p. 136
4.8.1	Model 1a	p. 136
4.8.2	Model 1b	p. 139
4.8.3	Model 2a	p. 141
4.8.4	Model 2b	p. 143
4.8.5	Model 2c	p. 145
4.8.6	Model 2d	p. 151
4.9	Discussion & Conclusions	p. 155
Chapter 5: Eastern Succession			p. 160
	<i>Abstract</i>	p. 161
5.1	General Introduction	p. 162
5.2	Background Geology	p. 163
5.2.1	Mount Isa Block	p. 163
5.2.2	Eastern Fold Belt	p. 166
5.2.3	Intrusive History	p. 168
5.2.4	Tectonic History & Metallogenesis	p. 169
5.2.5	Prospectivity	p. 173
5.3	Conceptual Models	p. 173
5.3.1	Methodology & Conceptual Models	p. 174
5.4	Numerical Modelling	p. 179
5.4.1	Modelling Approach	p. 179
5.4.2	UDEC	p. 180
5.4.3	Sensitivity Analysis	p. 181
5.4.4	Boundary Conditions & Model Parameters	p. 186
5.5	Results Model 1	p. 189
5.5.1	Model 1a	p. 190
5.5.2	Model 1b	p. 195
5.5.3	Model 1c	p. 200
5.5.4	Model 1d	p. 205
5.6	Results Model 2	p. 210
5.6.1	Model 2a	p. 210
5.6.2	Model 2b	p. 216
5.6.3	Model 2c	p. 220
5.6.4	Model 2d	p. 226
5.6.5	Aperture & Fluid Flow Behaviour	p. 231
5.6.6	Prospectivity & Mineralisation	p. 236
5.7	Discussions & Conclusions	p. 243

Chapter 6: Extension	p. 247
<i>Acknowledgements</i>	p. 248
<i>Abstract</i>	p. 249
6.1 Introduction	p. 251
6.2 Geological Context	p. 252
6.3 Numerical Modelling	p. 256
6.4 Extension and Basin Formation	p. 258
6.5 Conceptual Models	p. 258
6.6 Results	p. 260
6.6.1 Model 1a	p. 260
6.6.2 Model 1b	p. 262
6.6.3 Model 2a	p. 265
6.6.4 Model 2b	p. 268
6.6.5 Model 2c	p. 271
6.6.6 Model 2d	p. 274
6.6.7 Strain Rate Variations	p. 278
6.7 Discussion & Conclusions	p. 280
References	p. 284
 SECTION B		
Appendix 1 – FLAC numerical code		A1 – A86
Appendix 2 – UDEC numerical code		A87 – A131

LIST OF FIGURES

Chapter 2

Fig. 2.1.	Schematic diagrams of stress and strain.	p. 10
Fig. 2.2.	3-dimensional components of stress, and stress resolved into Cartesian co-ordinates.	p. 11
Fig. 2.3.	Schematic diagrams displaying vertical and horizontal stress components.	p. 13
Fig. 2.4.	Schematic diagram of continental crust sitting on a fluid mantle.	p. 14
Fig. 2.5.	Series of elastic-plastic stress strain curves.	p. 15
Fig. 2.6.	Schematic diagram indicating the Poisson effect for uniaxial applied force.	p. 16
Fig. 2.7.	Schematic diagrams indicating failure envelope relationships.	p. 20
Fig. 2.8.	Schematic 2-dimensional representation of yield surface and plastic strain increments.	p. 23
Fig. 2.9.	1-dimensional stress strain curves	p. 27
Fig. 2.10.	Representation of Darcy's experiment for porous media flow.	p. 30
Fig. 2.11.	Schematic representation of Darcy's and Forchheimer's equations for one dimensional flow.	p. 31
Fig. 2.12.	Mohr-circle analysis diagram.	p. 34
Fig. 2.13.	Dilatometric results from deformation experiments on Carrara marble.	p. 35
Fig. 2.14.	Microstructural interpretations of the dilation angle in geo-materials.	p. 36
Fig. 2.15	General solution procedure for the modelling process.	p. 43

Chapter 3

Fig. 3.1.	Schematic representations of hydrological cycles.	p. 54
Fig. 3.2.	Simplified regional geological map of the Pilbara Block, W.A.	p. 58
Fig. 3.3.	Simplified regional geological cross section of the Hamersley Province.	p. 60
Fig. 3.4.	Mechanical boundary conditions for all models.	p. 67
Fig. 3.5.	Starting conditions for four basic conceptual models.	p. 69

Fig. 3.6.	Conceptual model 5, the Hamersley model.	p.	70
Fig. 3.7.	Six variations of the reaction enhanced permeability function applied to the Hamersley models.	p.	71
Fig. 3.8.	Two stages of the permeability change in BIF layers.	p.	72
Fig. 3.9.	Plot of hydraulic head and Darcy flow vectors for Model 1.	p.	73
Fig. 3.10.	Plot of pore pressure and Darcy flow vectors of Model 2 at 3% deformation.	p.	74
Fig. 3.11.	Plot of pore pressure, hydraulic head, volumetric strain and Darcy flow vectors of Model 3 at 3% deformation.	p.	75
Fig. 3.12.	Plot of pore pressure and Darcy flow vectors of Model 4 at 3% and 7% deformation.	p.	77
Fig. 3.13.	Plot of pore pressure and Darcy flow vectors of Model 5 at 3% deformation.	p.	78
Fig. 3.14.	Plot of pore pressure, plasticity and Darcy flow vectors of Model 5 at 10% deformation.	p.	79
Fig. 3.15.	Plot of pore pressure and Darcy flow vectors of Model 6 at 3% deformation.	p.	80
Fig. 3.16.	Plot of pore pressure and Darcy flow vectors of Model 6 at 10% deformation.	p.	81

Chapter 4

Fig. 4.1.	Map of northern Australia, Mt Isa terrain and Pb-Zn-Ag deposits.	p.	89
Fig. 4.2.	Chronostratigraphic framework for the Mt Isa terrain.	p.	90
Fig. 4.3.	Stratigraphic Column and Superbasins of the Western Fold Belt.	p.	98
Fig. 4.4.	Stratigraphic summary of the Western Fold Belt and McNamara Group.	p.	99
Fig. 4.5.	Stratigraphy of the Lawn Hill Platform.	p.	100
Fig. 4.6.	Stratigraphic Column comparing classification schemes.	p.	103
Fig. 4.7.	Stratigraphic summary and description of the Century deposit.	p.	107
Fig. 4.8a.	Digital Terrain Model of Century regional structures.	p.	115
Fig. 4.8b.	Digital Terrain Model of local structures at Century.	p.	115
Fig. 4.9.	Digital Terrain Model integrated with pit-scale structures.	p.	116

Fig. 4.10a.	3-D Thickness maps looking South.	p.	117
Fig. 4.10b.	3-D Thickness maps looking North.	p.	118
Fig. 4.11a.	3-D Pb distributions looking North.	p.	121
Fig. 4.11b.	3-D Pb distributions looking South.	p.	122
Fig. 4.12a.	3-D Zn distributions looking North.	p.	123
Fig. 4.12a.	3-D Zn distributions looking South.	p.	124
Fig. 4.13.	Conceptual Models (Model1 and Model2).	p.	132
Fig. 4.14.	Century cross section	p.	134
Fig. 4.15.	Model 1a (1%) - Plots of pore pressure, permeability, and fluid flow.	p.	137
Fig. 4.16.	Model 1a (2%) - Pressure gradient graph, pore pressure and fluid flow.	p.	138
Fig. 4.17.	Model 1b (1%) - Plots of pore pressure, permeability, and fluid flow.	p.	140
Fig. 4.18.	Model 1b (2%) - Plot of pore pressure, and fluid flow.	p.	141
Fig. 4.19.	Model 2a (2%) - Plot of pore pressure, and fluid flow. Graph of pp v time.	p.	142
Fig. 4.20.	Model 2a (3% - 9%) - Plot of pore pressure, volumetric strain and fluid flow.	p.	144
Fig. 4.21.	Model 2a (9%) - Plot of volumetric strain and fluid flow.	p.	145
Fig. 4.22.	Model 2b - Plots of pore pressure, and fluid flow.	p.	146
Fig. 4.23.	Model 2b (3% - 5%) - Plots of pore pressure, volumetric strain and fluid flow.	p.	147
Fig. 4.24.	Model 2b (9%) - Plot of volumetric strain and fluid flow.	p.	148
Fig. 4.25.	Model 2c (1%) - Plots of pore pressure, permeability, and fluid flow.	p.	149
Fig. 4.26.	Model 2c (1% - 5%) - Plots of volumetric strain and fluid flow.	p.	150
Fig. 4.27.	Model 2d (3%) - Plots of pore pressure, volumetric strain and fluid flow.	p.	152
Fig. 4.28.	Model 2d (3% - 5%) - Plots of permeability, yield state, volumetric strain and fluid flow.	p.	153
Fig. 4.29.	Model 2d (7%) - Plots of volumetric strain and fluid flow.	p.	155

Chapter 5

Fig. 5.1.	General geology and location map of the Mount Isa Block.	p.	164
Fig. 5.2.	Detailed geological map of the Eastern Fold Belt and study area.	p.	175
Fig. 5.3.	Conceptual model and boundary conditions for Model 1.	p.	176
Fig. 5.4.	Conceptual model and boundary conditions for Model 2.	p.	177
Fig. 5.5.	Conceptual models for sensitivity testing of smooth versus sharp geometrical bends.	p.	182
Fig. 5.6.	UDEC results of sensitivity testing of geometrical features.	p.	183
Fig. 5.7.	UDEC results of sensitivity testing of four variations in friction angle values.	p.	184
Fig. 5.8.	UDEC results of sensitivity testing of stiffness parameters of fractures.	p.	185
Fig. 5.9.	UDEC plot of unbalanced history at approx 1500 cycles for Model 1.	p.	188
Fig. 5.10.	Mohr diagram with failure envelopes representing granite, metasediments and faults.	p.	188
Fig. 5.11.	Plots of mean stress for Model 1a.	p.	191
Fig. 5.12.	Plots of volumetric strain and minor principal stress for Model 1a.	p.	192
Fig. 5.13.	Plots of differential stress for Model 1a.	p.	193
Fig. 5.14.	Plots of fluid pressure required for failure for Model 1a.	p.	194
Fig. 5.15.	Plots of mean stress for Model 1b.	p.	196
Fig. 5.16.	Plots of minor principal stress for Model 1b.	p.	197
Fig. 5.17.	Plots of differential stress for Model 1b.	p.	198
Fig. 5.18.	Plots of fluid pressure required for failure for Model 1b.	p.	199
Fig. 5.19.	Plots of mean stress for Model 1c.	p.	201
Fig. 5.20.	Plots of minor principal stress for Model 1c.	p.	202
Fig. 5.21.	Plots of differential stress for Model 1c.	p.	203
Fig. 5.22.	Plots of fluid pressure required for failure for Model 1c.	p.	204
Fig. 5.23.	Plots of mean stress for Model 1d.	p.	206
Fig. 5.24.	Plots of minor principal stress for Model 1d.	p.	207

Fig. 5.25.	Plots of differential stress for Model 1d.	p.	208
Fig. 5.26.	Plots of fluid pressure required for failure for Model 1d.	p.	209
Fig. 5.27.	Plots of mean stress for Model 2a.	p.	211
Fig. 5.28.	Plots of volumetric strain and minor principal stress for Model 2a.	p.	212
Fig. 5.29.	Plots of differential stress for Model 2a.	p.	214
Fig. 5.30.	Plots of fluid pressure required for failure for Model 2a.	p.	215
Fig. 5.31.	Plot of mean stress for Model 2b.	p.	216
Fig. 5.32.	Plots of minor principal stress for Model 2b.	p.	217
Fig. 5.33.	Plots of differential stress for Model 2b.	p.	218
Fig. 5.34.	Plots of fluid pressure required for failure for Model 2b.	p.	219
Fig. 5.35.	Plot of mean stress for Model 2c.	p.	222
Fig. 5.36.	Plots of minor principal stress for Model 2c.	p.	223
Fig. 5.37.	Plots of differential stress for Model 2c.	p.	224
Fig. 5.38.	Plots of fluid pressure required for failure for Model 2c.	p.	225
Fig. 5.39.	Plot of mean stress for Model 2d.	p.	227
Fig. 5.40.	Plots of minor principal stress for Model 2d.	p.	228
Fig. 5.41.	Plots of differential stress for Model 2d.	p.	229
Fig. 5.42.	Plots of fluid pressure required for failure for Model 2d.	p.	230
Fig. 5.43.	Plots of joint hydraulic aperture, flow rates and velocities.	p.	232
Fig. 5.44.	Volumetric flow rates.	p.	234
Fig. 5.45.	Plots of aperture widths and mean stress.	p.	235
Fig. 5.46.	Plasticity state comparison of regional Model 2a and Model 2b.	p.	238
Fig. 5.47.	Plasticity state comparison of regional Model 2c and Model 2d.	p.	239
Fig. 5.48.	Plasticity state comparison of Selwyn region Model 2c and Model 2d.	p.	240
Fig. 5.49.	Regional comparison with prospectivity analysis by Mustard <i>et al.</i> , 2004.	p.	241
Fig. 5.50.	Selwyn region comparison with prospectivity analysis by Mustard <i>et al.</i> , 2004.	p.	242

Chapter 6

Fig. 6.1.	Conceptual models of four basic geometries.	p.	259
Fig. 6.2.	Model 1a - Plots of unbalanced force and shear strain rate (2%) for Model 1a.	p.	261
Fig. 6.3.	Model 1a (6%) - Plots of shear strain rates, pore pressure, and fluid flow.	p.	262
Fig. 6.4.	Model 1b (2%) - Plots of pore pressure, shear strain rates, and fluid flow.	p.	263
Fig. 6.5.	Model 1b (6%) - Plots of pore pressure, and fluid flow.	p.	264
Fig. 6.6.	Model 2a (2%) - Plots of shear strain rates, pore pressure, and fluid flow.	p.	265
Fig. 6.7.	Model 2a (2%) - Plot of pore pressure, and fluid flow.	p.	266
Fig. 6.8.	Model 2a (2%) - Plots of pore pressure, and fluid flow.	p.	267
Fig. 6.9.	Model 2a (6%) - Plots of pore pressure, plasticity state and fluid flow.	p.	268
Fig. 6.10.	Model 2b (2%) - Plots of shear strain rates, pore pressure, and fluid flow.	p.	269
Fig. 6.11.	Model 2b (6%) - Plots of pore pressure, permeability and fluid flow.	p.	270
Fig. 6.12.	Model 2c (2%) - Plots of shear strain rates, pore pressure, and fluid flow.	p.	271
Fig. 6.13.	Model 2c (2%) - Plots of pore pressure, shear strain rate and fluid flow.	p.	272
Fig. 6.14.	Model 2c (6% - 8%) - Plots of pore pressure, and fluid flow.	p.	273
Fig. 6.14c	Model 2c (10%) - Plot of pore pressure, and fluid flow.	p.	274
Fig. 6.15.	Model 2d (2%) - Plots of shear strain rates and fluid flow.	p.	275
Fig. 6.16.	Model 2d (2%) - Plots of pore pressure, volumetric strain and fluid flow.	p.	276
Fig. 6.17.	Model 2d (2%) - Plots of pore pressure and fluid flow.	p.	277

LIST OF TABLES**Chapter 3**

Table 3.1 Material properties for numerical models. p. 68

Chapter 4

Table 4.1 Correlation of Deformational Events and Geochronology. p. 95

Table 4.2 Physical properties for materials for Models 1 and 2. p. 133

Chapter 5

Table 5.1 Physical properties of rocks, contacts and faults. p. 189

Chapter 6

Table 6.1 Material properties for FLAC coupled deformation and fluid flow models. p. 259

LIST OF SYMBOLS

A	cross sectional area (m)
b	aperture (m)
c	cohesion (Pa)
e	void ratio
E	youngs modulus (Pa)
F	yield function for plasticity models
F_c	horizontal force in the crust (N m^{-1})
g	gravitational acceleration (9.81m s^{-2})
G	shear modulus (Pa)
h	height (m)
H	hydraulic head (m)
k	permeability (m^2)
k_{ij}	permeability tensor (m^2)
k_n	normal stiffness of joints (Pa)
K	hydraulic conductivity (m s^{-1})
K	elastic bulk modulus (Pa)
K_f	Bulk modulus of fluid
K_s	Bulk modulus of solid
L	length (m)
M	slope of critical state line
M_f	Biot modulus for fluid
M_s	Biot modulus for solid
n	porosity
N	number of joints per unit distance
p_c	yield surface intercept (strain hardening/softening)
p_f	pore fluid pressure (Pa)
Pf	fluid pressure (Pa)
P	pressure (Pa)
PF_f	fluid pressure required for failure (Pa)
q	specific discharge
Q	flow potential function for plasticity models
Q	volumetric fluid flow rate ($\text{m}^3 \text{s}^{-1}$)
Re	Reynolds number for porous media
Rk	Stiffness ratio

T	tensile strength (Pa)
v	poissons ratio
v	specific volume ($\text{m}^3 \text{kg}^{-1}$)
v	kinematic viscosity ($\text{m}^2 \text{s}^{-1}$)
V_i	Darcy fluid velocity (m s^{-1})
V_v	void volume (m^3)
V_t	total volume (m^3)
V_s	volume of the solid (m^3)
w	fracture width (m)
z	elevation (m)
α	angle of shear ($^\circ$)
β	yield surface parameter for modified Cam-Clay plasticity
ε_a	axial strain
ε_n	normal strain
$\underline{\varepsilon}^{pl}$	plastic strain
ε_v^p	plastic volumetric strain
ε_r	radial strain
ε_s	shear strain
ε_{xx}	normal strain in the x plane
ε_{yy}	normal strain in the y plane
ε_{xy}	shear strain on x plane in y direction
ε_{yx}	shear strain on y plane in x direction
ϕ	friction angle ($^\circ$)
γ	shear strain
γ_f	specific weight ($\text{kg m}^{-2} \text{s}^{-2}$)
γ_p	rate of plastic shear strain
μ	viscosity ($\text{kg m}^{-1} \text{s}^{-1}$), (Pa s)
μ	friction coefficient
ρ	density (kg m^{-3})
ρ_c	density of the crust (kg m^{-3})
ρ_m	density of the mantle (kg m^{-3})
ρ_w	density of fluid (kg m^{-3})
η	dynamic viscosity (Pa s)
η_f	viscosity ($\text{kg m}^{-1} \text{s}^{-1}$), (Pa s)
σ_c	critical stress (Pa)
σ_{eff}	effective stress (Pa)
σ_m	mean stress (Pa)
σ_n	normal stress (Pa)

σ_0	yield stress (Pa)
σ_s	shear stress (Pa)
$\sigma_{x,y,z}$	normal stress components (Pa)
σ_{xx}	normal stress in the x plane (Pa)
σ_{yy}	normal stress in the y plane (Pa)
σ_{xy}	shear on the x plane in the y direction (Pa)
σ_{yx}	shear on the y plane in the x direction (Pa)
σ_1	maximum principal stress (Pa)
σ_2	intermediate principal stress (Pa)
σ_3	minimum principal stress (Pa)
σ^*	mean stress (Pa)
$\underline{\sigma}$	stress tensor
$\bar{\sigma}$	effective stress (Pa)
τ	shear stress (Pa)
τ_s	shear stress (Pa)
τ^*	maximum shear stress (Pa)
t	deviatoric stress measure (Pa)
$\Delta\sigma$	differential stress (Pa)
$\Delta\sigma_n$	effective normal stress increment (Pa)
$\Delta\mu_n$	normal displacement increment (Pa)
π	pi
ψ	dilation angle (°)
Ψ	hardening parameter